

PHOTONICS Research

Slow-light-enhanced on-chip 1D and 2D photonic crystal waveguide gas sensing in near-IR with an ultrahigh interaction factor

ZIHANG PENG,¹ YIJUN HUANG,¹ KAIYUAN ZHENG,² CHUANTAO ZHENG,^{1,*}  MINGQUAN PI,¹ HUAN ZHAO,¹ JIALIN JI,¹ YUTING MIN,¹ LEI LIANG,³ FANG SONG,¹ YU ZHANG,¹ YIDING WANG,¹ AND FRANK K. TITTEL⁴

¹State Key Laboratory of Integrated Optoelectronics, College of Electronic Science and Engineering, Jilin University, Changchun 130012, China

²Department of Electrical Engineering and Photonics Research Institute, The Hong Kong Polytechnic University, Hong Kong 518060, China

³State Key Laboratory of Luminescence and Applications, Changchun Institute of Optics, Fine Mechanics and Physics, Chinese Academy of Sciences, Changchun 130033, China

⁴Department of Electrical and Computer Engineering, Rice University, Houston, Texas 77005, USA

*Corresponding author: zhengchuantao@jlu.edu.cn

Received 5 May 2023; revised 25 July 2023; accepted 26 July 2023; posted 28 July 2023 (Doc. ID 494762); published 21 September 2023

Nanophotonic waveguides hold great promise to achieve chip-scale gas sensors. However, their performance is limited by a short light path and small light–analyte overlap. To address this challenge, silicon-based, slow-light-enhanced gas-sensing techniques offer a promising approach. In this study, we experimentally investigated the slow light characteristics and gas-sensing performance of 1D and 2D photonic crystal waveguides (PCWs) in the near-IR (NIR) region. The proposed 2D PCW exhibited a high group index of up to 114, albeit with a high propagation loss. The limit of detection (LoD) for acetylene (C_2H_2) was 277 parts per million (ppm) for a 1 mm waveguide length and an averaging time of 0.4 s. The 1D PCW shows greater application potential compared to the 2D PCW waveguide, with an interaction factor reaching up to 288%, a comparably low propagation loss of 10 dB/cm, and an LoD of 706 ppm at 0.4 s. The measured group indices of the 2D and 1D waveguides are 104 and 16, respectively, which agree well with the simulation results. © 2023 Chinese Laser Press

<https://doi.org/10.1364/PRJ.494762>

1. INTRODUCTION

Gas detection has wide applications in fields such as industrial process control, environmental monitoring, and medical diagnosis. Many gas sensors have been proposed in the current scenario [1–3]. Among these, an IR absorption spectroscopy-based gas sensor is considered as one of the most promising due to its capability to identify distinct gas species and measure their concentration levels with high sensitivity, a short response time, and real-time as well as remote monitoring ability. It is the unique “fingerprint areas” in the IR band that facilitate this precision [4–7]. Over the past few years, on-chip gas sensors based on optical waveguides, such as chalcogenide glass waveguides [8], silicon-on-insulator (SOI) waveguides [9–11], silicon-on-silicon nitride (SON) waveguides [12], silicon-on-sapphire (SOS) waveguides [13], and Ta_2O_5 waveguides [14], have attained considerable progress. Compared to the gas sensors based on discrete optical devices, on-chip waveguide sensors eliminate the need for large gas chambers and complex optical alignment. Notably, the integration of a passive waveguide with a laser and a photodetector on a single chip [15–17] has enabled the realization of miniaturized and ultracompact

gas sensors. Optical waveguide sensors show great potential, especially in distributed sensors and large-scale sensor network deployment.

The principle of the IR absorption spectroscopy of the on-chip sensor also obeys Beer–Lambert law, and the absorbance of gas molecules can be expressed as $A = \gamma\alpha CL$, where γ is the interaction factor of the waveguide, α is the absorption coefficient, C is the gas concentration, and L is the waveguide length. According to the perturbation theory [18], $\gamma = f \times n_g$, where f is the overlap factor between the electric field and gas, n_g is the group index of the waveguide mode, denoting the slowing factor of light. IBM has reported a new sensor to detect methane (CH_4) through absorption spectroscopy, based on a near-IR silicon photonic waveguide with a 10 cm silicon strip and a limit of detection (LoD) of 772 ppm (parts per million) [19]. However, the performance of optical waveguide sensors is limited due to the short optical length and weak evanescent field intensity. To improve the performance, various methods have been proposed to increase γ , which is related to the sensitivity of the sensor. In our previous work, we used a suspended slot chalcogenide waveguide [20] and silver island film [21] to enhance absorption. Furthermore, suspended waveguides [22] can

achieve a greater overlap factor f , while photonic crystal waveguides (PCWs) and subwavelength grating waveguides (SWG) with larger n_g have replaced traditional strip waveguides [23–26]. Most of the existing reports focus on the mid-IR (MIR), where optical instruments are expensive and bulky, making them unsuitable for packaging, integration, and field applications. Moreover, rotating the waveguide mode may be necessary for certain MIR waveguide sensors [27,28], which leads to extra loss and more complicated optical calibration. Despite the low cost of near-IR (NIR) optical components, the application of on-chip gas sensors in NIR is limited because the absorption of most gases in the NIR region is more than one order of magnitude weaker than that in the MIR. A slotted photonic crystal waveguide has been shown to be feasible for NIR methane detection [29], simultaneously exhibiting considerable f and n_g . However, its propagation loss is about three times that of ordinary PCWs [30], which negatively impacts the on-chip sensor's performance.

1D PCWs have been shown to generate slow light effects like 2D PCWs because of their strong structural dispersion. These waveguides are widely used for refractive index sensing of liquids or chemicals due to highly correlated transmittance with a wavelength [31–33]. Nevertheless, since gas analytes have a refractive index slightly higher than that of air [34,35], refractive index sensing is unapplicable for their detection. To achieve enhanced sensitivity in NIR detection, we developed a 2D PCW with a non-slot structure featuring a group index of up to 114 and an impressive interaction factor of 6.84. Concurrently, the theoretical and experimental investigations of the slow light characteristics and gas-sensing performance using IR absorption spectroscopy of a 1D PCW were conducted. Although the 2D PCW demonstrates a superior

detection sensitivity at a 1 mm length, it is important to consider the propagation loss in the context of deploying large-scale sensor networks and optimal performance achievement. Consequently, the 1D PCW remains a favorable choice because of its low propagation loss. Additionally, it is anticipated that a 1 cm length 1D PCW could achieve an LoD of tens of ppm in the NIR. Our research focuses on the detection of acetylene (C_2H_2) as the target gas.

2. DEVICE DESIGN

A. 2D PCW

We selected an SOI platform as the medium to design the PCWs due to its high refractive index difference between the core and cladding materials, which is conducive to the creation of photonic band gaps in a photonic crystal. In Figs. 1(a) and 1(b), we present a 3D structure diagram of the 2D PCW, which comprises a hexagonal lattice photonic crystal structure with a lattice constant of a and a waveguide width of $W1.1$. At its center, a row of bulk holes with a radius of R along the $\Gamma - K$ direction is replaced by smaller ones with a radius of r_0 . Note that the 2D PCW offers a TE band gap at a low frequency band; hence, we exclusively explore its slow light characteristics in the context of TE polarized light. The extent of the bandgap frequency range of the 2D photonic crystal slab depends on both the thickness of the slab h and R . Therefore, to secure a wide band gap below the light line, we kept R fixed at $0.25a$, while h was set at 220 nm.

Figure 1(c) displays a typical dispersion diagram of a PCW when the background materials are pure C_2H_2 and air, respectively; at room temperature and atmospheric pressure, the refractive index of pure C_2H_2 is approximately 3.24×10^{-4}

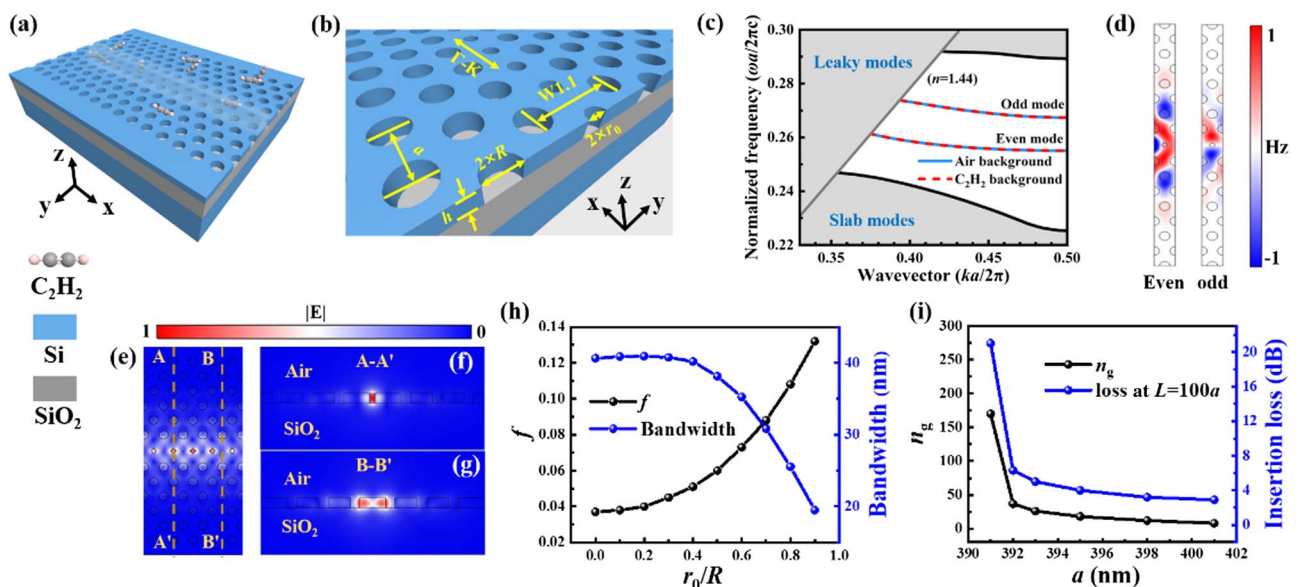


Fig. 1. (a) 3D schematic of the 2D PCW with a 220 nm thick Si layer and a 2 μm thick BOX layer. (b) Geometric parameters of the 2D PCW including the lattice constant a , radius of bigger air holes R , radius of center defect holes r_0 , waveguide width $W1.1$, thickness of Si h , and direction of the defect $\Gamma - K$. (c) Dispersion diagram under air and pure C_2H_2 background with $R = 0.25a$ and $r_0 = 0.5R$. (d) Hz distributions of even mode and odd mode when $ka/2\pi = 0.5$. (e) $|E|$ distribution of the even mode at a wavelength of 1532.83 nm. $|E|$ distributions (f) at the cross section through a defect hole and (g) through Si slab in (e). (h) Guided mode bandwidth below the SiO_2 light line in terms of wavelength (nm) and f versus r_0/R ratio. (i) Simulated curves of group index and insertion loss versus the lattice constant.

higher than that of air (1.000273) [34,35]. The guided mode shows no shift under a pure C_2H_2 background. Thus, the introduction of C_2H_2 with different concentration levels will not change the band structure or mode of the PCW, excluding the influence on the absorption signal. The dark gray solid line denotes the light line, above which the propagation of light is prevented in the central region of the PCW due to significant vertical leakage loss. The guided modes within the band gap are distinguished from the slab modes by positive stop gaps, delineated by solid blue lines. The Hz components of the guided modes are symmetrically and antisymmetrically distributed along the center of the PCW, and named even and odd modes, respectively, as shown in Fig. 1(d). Odd TE modes in the PCW can be excited by higher-order modes with an odd Hz field in the strip waveguide that coupled to the PCW. This means that additional mode converters must be designed carefully to ensure the existence of higher-order modes. But an even mode in the PCW can be directly excited using the fundamental mode in the strip waveguide without mode conversion, so we select the even mode to customize the waveguide sensor [36,37]. The electric field intensity profiles of the even mode in the horizontal and vertical cross sections of the 2D PCW are illustrated in Figs. 1(e)–1(g). The photonic band gap effect localizes the energy to the central region, possessing a width of $1.1 \times \sqrt{3}a$, and enhances the electric field intensity in the defect holes compared to the silicon slab. The filling factor f , which is a critical index determining the interaction between the waveguide and gas that represents the proportion of analyte energy to the entire volume energy, is defined as

$$f = \frac{\iiint_{\text{air}} (n_{\text{gas}}^2 |E_{\text{gas}}|^2) dV}{\iiint_{\text{total}} (n_{\text{gas}}^2 |E_{\text{gas}}|^2 + n_{\text{slab}}^2 |E_{\text{slab}}|^2 + n_{\text{clad}}^2 |E_{\text{clad}}|^2) dV}. \quad (1)$$

The integral lying on the numerator denotes the fraction of mode power that interacts with the analytes, whereas the integral at the denominator is the mode power in the whole volume. n_{gas} is the refractive index of gas analyte, and n_{slab} is the refractive index of the silicon layer. n_{clad} is the refractive index of the lower cladding material; i.e., silicon dioxide. E_{gas} , E_{slab} , and E_{clad} are the electric field intensity in, respectively, gas, Si slab, and SiO_2 .

Figure 1(h) illustrates the curve of the even mode bandwidth lying below the SiO_2 light line, presented as a function of the normalized frequency ($\omega a/2\pi c$) and the filling factor with respect to r_0/R . During the fabrication of a PCW, the guided mode may encounter a shift, owing to the occurrence of fabrication errors, and moderate side wall roughness causes a loss to mode propagation. Consequently, if the bandwidth is narrow, there is a likelihood that the light that was initially positioned on the guide mode will fall into the stop gap. To accurately ascertain the regime of slow-light transmission of the guided mode, it is crucial to ensure a large guiding bandwidth for the optimized 2D PCW. Moreover, a large f must also be ensured, thereby making the choice of $r_0 = 0.5R$ the optimal design.

To detect C_2H_2 in NIR, the target wavelength was set to 1532.83 nm, where the absorption coefficient $\alpha = 1.037 \text{ cm}^{-1}$.

To achieve a high interaction factor at $\lambda = 1532.83 \text{ nm}$, it is crucial to ensure a large group index. However, slow light PCWs exhibit transmission loss proportional to their group index, and excessive loss can adversely affect the SNR of the sensor. To strike a balance between these factors, we optimized the group index of the 2D PCWs by carefully selecting an appropriate lattice constant. Figure 1(i) illustrates the group index of the 2D PCW under varying lattice constants. As the lattice constant a increases, the group index gradually decreases. When $a = 390 \text{ nm}$, the target wavelength aligns with the photonic bandgap. Additionally, we employed a 3D finite-difference time-domain (FDTD, Ansys Lumerical) method to simulate the insertion loss of the 2D PCW, considering different group indices when the length $L = 100a$, $R = 0.25a$, and $r_0 = 0.5R$, as shown in Fig. 1(i). The primary source of insertion loss stems from the mode field mismatch between the coupled strip waveguide and the PCW. Consequently, a higher n_g exacerbates this mismatch, resulting in a more significant insertion loss. Therefore, we opted for a lattice constant of 392 nm in this design, which ensured a relatively large n_g while maintaining an acceptable level of insertion loss.

B. 1D PCW

The schematic of the 1D PCW is shown in Fig. 2(a). It is composed of periodically etched air holes in a strip waveguide with a thickness of 220 nm and a width of w . Unlike the 2D PCW, the 1D PCW is only periodic in the propagation direction; in the y and z directions, light is localized in the waveguide by total internal reflection. The periodicity of the x direction leads to the appearance of incomplete photonic band gaps, in which no guided mode exists. Figure 2(b) shows the dispersion diagram of the 1D PCW with a period of a_s and the background materials are pure C_2H_2 and air, when the holes have a radius $R_s = 0.25a_s$ and waveguide width $w = 1.6a_s$. Similarly, the guided mode shows no shift under a pure C_2H_2 background. There are four TE bands below the SiO_2 light line, and each one can serve as a guided mode. The Hz distribution of the four modes is presented in Fig. 2(c), where modes 1 and 2 are even modes while modes 3 and 4 are odd modes. Figures 2(d)–2(f) illustrate the electric field intensity distribution of mode 1 in the horizontal and vertical cross sections of the 1D PCW, and Figs. 2(g)–2(i) exhibit that of mode 2. It is discernible that the electric field of mode 2 is primarily concentrated in the air holes, which is advantageous to enhance gas absorption. The filling factors of modes 1 and 2 are 4% and 15%, respectively; thus, mode 2 is intended for the waveguide sensor. The radius R_s and waveguide width w are optimized based on the filling factor and guided mode bandwidth. The plot in Fig. 2(j) illustrates the bandwidth below the SiO_2 light line in terms of normalized frequency ($\omega a/2\pi c$) and f plotted against w/a_s , when $R_s = 0.24a_s$, as well as R_s/a_s when $w = 1.5a_s$. f increases with an increase in R_s and a decrease in w , while the bandwidth has an opposite situation. The final results indicate that a compromise between f and guided bandwidth is achieved at $R_s = 0.25a_s$ and $w = 1.5a_s$. Figure 2(k) shows the group index and corresponding insertion loss of the 1D PCW under varying lattice constants, when the length $L = 100a_s$. Similar results can be obtained to that of the 2D PCW regarding the relation between group index and insertion loss. $a_s = 407 \text{ nm}$ is chosen

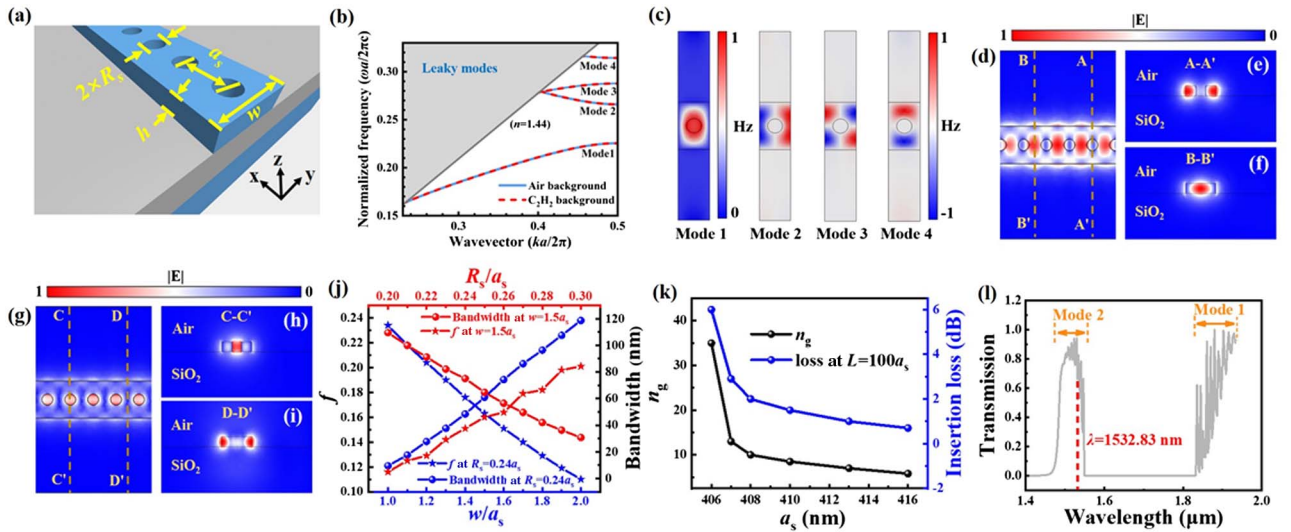


Fig. 2. (a) Geometric parameters of the 1D PCW including the lattice constant a_s , radius of air holes R_s , waveguide width w , and thickness of Si layer h . (b) Dispersion diagram under air and pure C_2H_2 background when $R_s = 0.24a_s$ and $w = 1.6R_s$. (c) $|E|$ distributions of the four modes in (b) at $ka_s/2\pi = 0.5$. $|E|$ distributions of mode 1 (d) at the horizontal section, (e) at vertical section through an air hole, and (f) through Si slab when the wavelength is 1532.83 nm. $|E|$ distributions of mode 2 (g) at the horizontal section, (h) at vertical section through an air hole, and (i) through Si slab when the wavelength is 1532.83 nm. (j) Guided mode bandwidth and f versus w/a_s when $R_s = 0.24a_s$, and versus R_s/a_s when $w = 1.5a_s$. (k) Simulated curves of the group index and insertion loss versus the lattice constant a_s . (l) Simulated transmission of the optimized 1D PCW.

as the optimal value in this case. We simulated the transmission of the optimized 1D PCW. As shown in Fig. 2(l), mode 1 shows a higher transmittance at longer wavelengths (1830–1930 nm), while mode 2 demonstrates a higher transmittance at shorter wavelengths (1470–1547 nm). The target wavelength 1532.83 nm is located in the slow light region of mode 2, which ensures the excitation of mode 2 in an experiment.

C. Grating Coupler

To achieve good coupling between optical fibers and the PCWs, we designed a subwavelength grating (SWG) coupler that requires just one etching step and can be fabricated simultaneously with the PCWs. Figure 3(a) shows the schematic of the SWG coupler, featuring an array of air trenches. Based on the effective medium theory (EMT) [38], the SWG coupler can be deemed equivalent to the structure delineated in Fig. 3(b). To begin, we implemented 2D FDTD simulations to evaluate the coupling efficiency to air versus the grating period and the equivalent refractive index n_{sub} . These outcomes are presented in Fig. 3(c). The period of the grating is optimized to be 760 nm, and n_{sub} is 2.45. The duty cycle ($L_{\text{sub}}/\text{period}$) is fixed at 50% during the optimization. Figure 3(d) shows the zeroth order approximation and the second order approximation of n_{sub} of the TE and TM modes versus the duty cycle f_{sub} of the air trench ($w_{\text{sub}}/P_{\text{sub}}$). For the zeroth order approximation of the TE mode, $n_{\text{sub}} = 2.45$ when $f_{\text{sub}} = 0.1$. Due to the incompatibility of the condition of the zeroth order approximation [39] with the accuracy of electron beam lithography (EBL), the second-order approximation is adopted. For the second-order approximation of the TE mode, the corresponding f_{sub} for $n_{\text{sub}} = 2.45$ is about 0.2. Consequently, w_{sub} is optimized to be 80 nm, and the period of the trench P_{sub} is 400 nm. Figure 3(e) shows the coupling

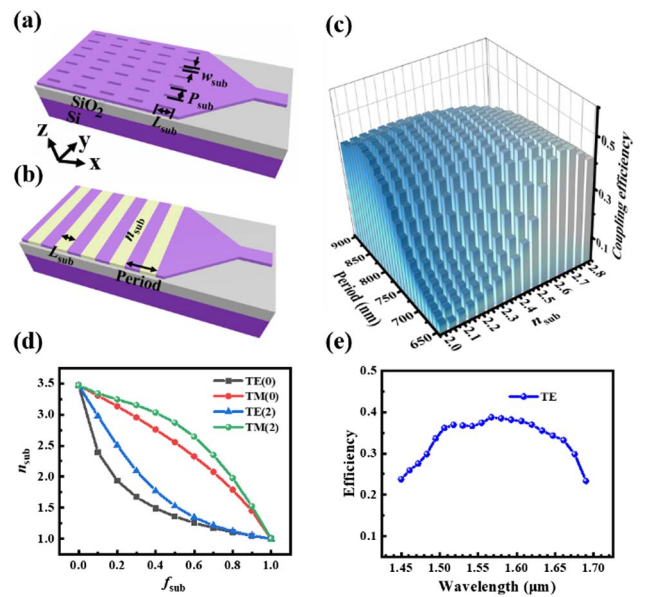


Fig. 3. (a) 3D schematic geometric parameters of the SWG coupler including the length L_{sub} , width w_{sub} , and period P_{sub} of the air trench. (b) Equivalent model of the SWG coupler including the period of the grating and equivalent refractive index n_{sub} . (c) Coupling efficiency to air versus period and n_{sub} . (d) Refractive index for different f_{sub} , calculated by EMT with zeroth-order and second-order approximations when $P_{\text{sub}} = 400$ nm. (e) Coupling efficiency simulated by 3D FDTD when $P_{\text{sub}} = 400$ nm, $w_{\text{sub}} = 80$ nm, period = 760 nm, and $L_{\text{sub}} = 380$ nm.

efficiency of the designed SWG coupler simulated by 3D FDTD. For $\lambda = 1532.83$ nm, the corresponding coupling efficiency is found to be 37%.

3. FABRICATION AND MEASUREMENT

Subsequently, we employed electron beam lithography (EBL) and inductively coupled plasma reactive ion etching (ICP-RIE) to fabricate the 2D PCW and 1D PCW on a commercially available SOI wafer with a top silicon layer with a 220 nm thickness and a buried oxide (BOX) layer with a 2 μm thickness. As depicted in Fig. 4 obtained from SEM, Fig. 4(a) illustrates the SWG coupler with dimensions of 17 μm in length and 10 μm in width, which matches with the core size of a single-mode fiber (SMF). Additionally, a tapered waveguide with a length of 500 μm is employed for mode transition, which is followed by a strip waveguide with a length of 500 μm . Figures 4(b) and 4(c) display the 2D and 1D PCW, respectively, and the same configuration is used for another port. Moreover, a transition zone was designed to reduce end reflection, as shown in Fig. 4(d). The diameter of air holes of the optimized 1D PCW is 204 nm. Considering that the minimum linewidth that can be etched is approximately 40 nm, the diameter of the air holes in the transition zone gradually increases from 44 nm to 204 nm, with a step size of 10 nm. Adjacent to both ends of the 1D PCW, 16 cycles of smaller holes form the transition zone. To measure the propagation loss and n_g , we fabricated both the 2D PCW and 1D PCW with varying lengths; namely, 200 μm , 600 μm , and 1000 μm . In addition, using the optimized fabrication

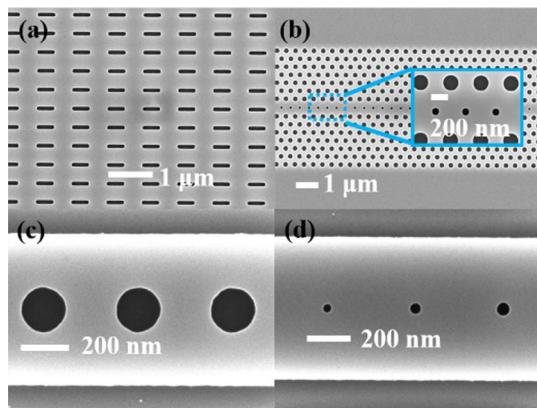


Fig. 4. SEM images for the fabricated (a) SWG coupler, (b) 2D PCW, (c) 1D PCW, and (d) mode transition zone in the 1D PCW.

parameters, no stiction was observed through SEM with the etching done.

The schematic of the gas measurement system is shown in Fig. 5. The light emission wavelength of the laser is tuned to 1532.83 nm by regulating the temperature controller and current controller. To mitigate low frequency noise in the system, an acousto-optic modulator (AOM) was implemented, modulating the intensity of the laser beam at a 40 kHz frequency. The beam is coupled to the chip via an SMF after passing through a polarization controller. During the testing procedure, a gas mixing system (Series 4000, Environics) was employed to mix pure nitrogen (carrier gas) and a standard C_2H_2 sample (concentration level 5%), resulting in varying concentration levels of the gas mixture. Subsequently, the prepared gas sample was conveyed to the chip surface using a gas tube made of polytetrafluoroethylene with a diameter of 0.125 in. (1 inch = 2.54 cm). The mixed gas was released at a height of approximately 0.2 mm from the chip surface, and then diffused into the holes of the PCWs. Both the gas concentration level and flow rate were determined by the gas mixing system. A flow rate of 200 standard cubic centimeters per minute (sccm) was set to ensure a consistent and stable absorption sensor signal. Moreover, a temperature control module with an accuracy of 0.01°C specially integrated on the chip holder was used to maintain the chip temperature at 20°C. A sine wave at the same frequency generated by the signal generator was used as the reference signal of the lock-in amplifier (LIA). The first harmonic signal demodulated by the LIA was harvested by the data acquisition.

Figure 6(a) shows the variations in light intensity over a 1 mm 2D PCW when exposed to pure N_2 and 5% C_2H_2 . A drop of approximately 4% is observed in the light intensity, with a sensor response time of 5.6 s and a recovery time of 4 s. The baseline drift in Fig. 6(a) may be caused by airflow disturbances as well as the gas dilution process. Although there appears to be some drift over a short period of time, it is noted that the baseline becomes relatively stable after a measurement duration of 12 min, as depicted in the insert in Fig. 6(c). Short-term measurements in Figs. 6(a) and 6(d) illustrate the dynamic testing process as well as the sensor's response time and recovery time. Note that the measured response time and recovery time of the sensor include the gas sample preparation time of the gas mixing system. Excluding this time, the sensor response time mainly depends on the gas flow rate and the gas diffusion speed

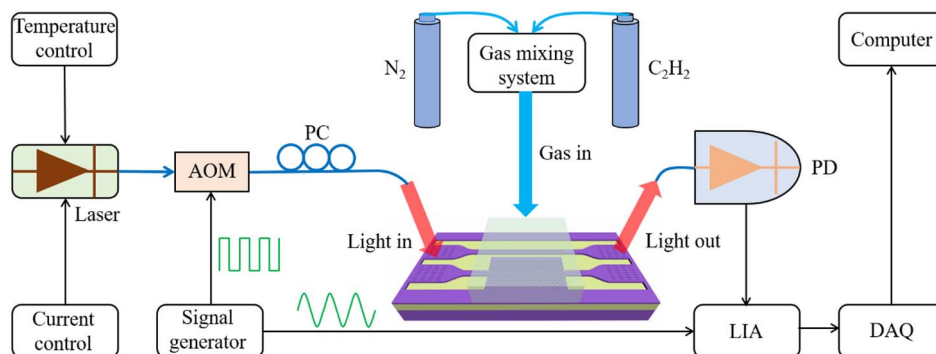


Fig. 5. Measurement setup. AOM, acousto-optic modulator; PC, polarization controller; PD, photodetector; LIA, lock-in amplifier; and DAQ: data acquisition.

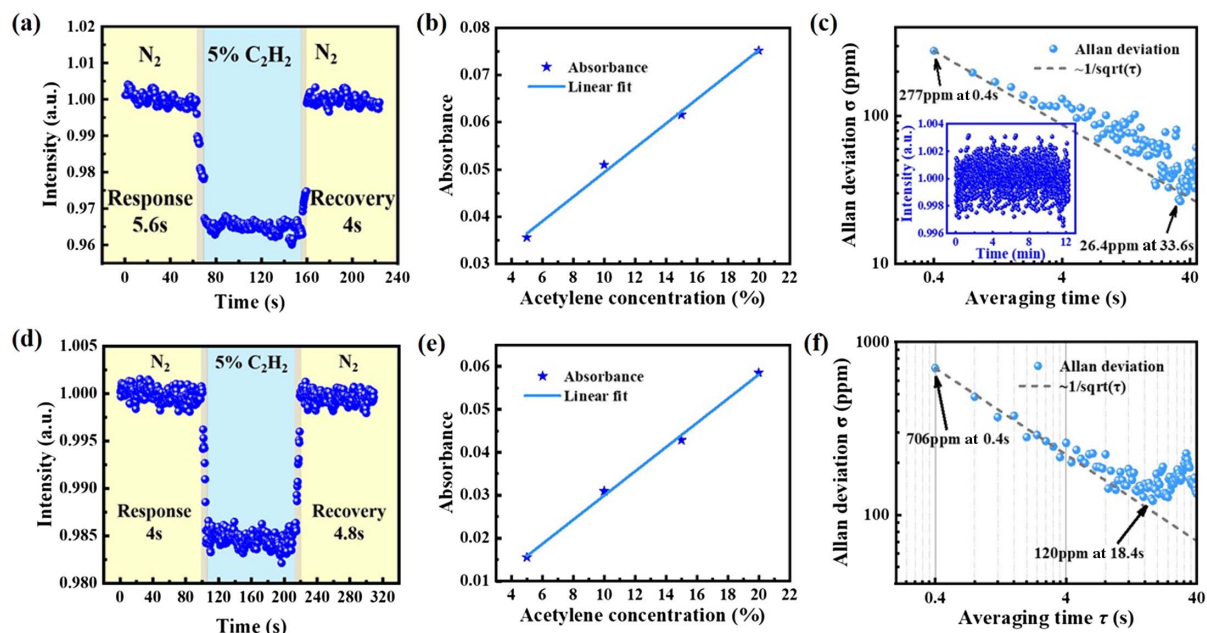


Fig. 6. (a) Measured transmitted light intensity through the 1 mm long 2D PCW when exposed to 5% C_2H_2 . (b) Absorbance of the 2D PCW sensor versus different concentration levels of C_2H_2 . (c) Allan deviation as a function of the averaging time τ ; the insert shows the baseline stability during a 12-minute measurement test. (d) Measured transmitted light intensity through the 1 mm long 1D PCW when exposed to 5% C_2H_2 . (e) Absorbance of the 1D PCW sensor versus different concentration levels of C_2H_2 . (f) Allan deviation as a function of the averaging time τ .

into the air holes. The sensor response can be sped up by increasing the gas flow rate. For practical application, the sensor chip also can be bonded to a gas cell, and the gas pressure in the cell can be increased to speed up the gas diffusion.

The absorbance of the 2D PCW at distinct concentration levels of C_2H_2 is plotted in Fig. 6(b). When investigating the gas absorption with varying concentration levels, we first introduced pure N_2 to the chip. After an approximate duration of 10 min, we proceeded to infuse the chip with 5% C_2H_2 for ~ 10 min, and then reintroduced pure N_2 . The identical process was subsequently employed to record the absorption signals of C_2H_2 at concentration levels of 10%, 15%, and 20%, respectively. The solid blue line shows a linear fit of absorbance, indicating high linearity of the sensor. To evaluate the minimum detectable acetylene concentration of the sensor, an Allan deviation analysis was performed on the data collected in a nitrogen environment, as shown in Fig. 6(c). In the measurement, the data sampling rate was set at 2.5 Hz, leading to an acquired data dot per 0.4 s. At an averaging time of 0.4 s, the sensor achieves a 1σ LoD of 277 ppm. An averaging time of 33.6 s brings down the 1σ LoD of the sensor to 24 ppm. The level of Gaussian white noise is indicated by the gray dashed line. At 0.4 s, the sensor is mainly dominated by Gaussian white noise. With an increase in the averaging time, the Gaussian white noise of the sensor is gradually suppressed, resulting in a decrease in the Allan deviation. The 2D PCW sensor reaches an optimal averaging time of 33.6 s, corresponding to the minimum noise level. After that, ultralow frequency noise and system drift dominate the sensor. Slight vibration of the optical platform and alignment drift between the fiber and grating couplers may result in system drift, consequently leading to a gradual increase in the Allan deviation.

An injection of 5% C_2H_2 into the 1D PCW with a length of 1 mm leads to a 1.5% drop in the sensor signal, as depicted in Fig. 6(d), with response and recovery times of 4 s and 4.8 s, respectively. The absorbance of the 1D PCW based sensor is plotted against varying C_2H_2 concentration levels in Fig. 6(e). In addition, the Allan deviation is calculated and displayed in Fig. 6(f), showing a 1σ LoD of 706 ppm. The minimum Allan deviation is achieved at 18.4 s, and the corresponding LoD is 120 ppm. The reason for the drift in the 2D and 1D PCW sensors is similar, which is due to the vibration and optical alignment change during measurements. To improve the Allan deviation, we can package the input/output fiber with the grating couplers to avoid a coupling position change, and the sensor can be immune to environmental vibration.

4. COMPARISON AND DISCUSSION

A. Absorption Analysis of PCWs and Strip Waveguide

To elucidate the characteristics of slow light in the PCWs, the absorbance caused by the strip waveguide was calculated. The strip waveguides connecting the 2D PCW and the 1D PCW have widths of 749 nm and 610 nm, respectively. In Figs. 7(a) and 7(b), the fundamental TE modes of their electric field intensity distribution are plotted. For the nondispersive structure, it is reasonable to assume that the effective refractive index n_{eff} is equal to the group index. For the 2D PCW, the external confinement factor f_c of the strip waveguide is 1.3%, and the n_{eff} is 2.65. The absorbance of the 1 mm long strip waveguide is calculated to be 0.00018 at 5% concentration of C_2H_2 , which corresponds to mere 0.45% of the total absorbance. The strip waveguide that connects the 1D PCW exhibits an

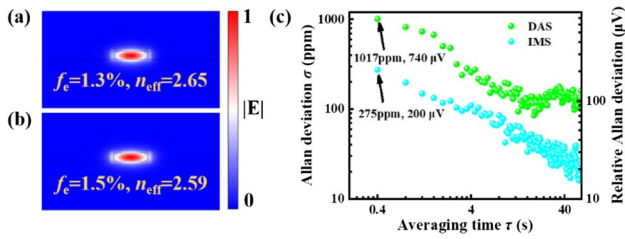


Fig. 7. $|E|$ distributions of the strip waveguide with a width of (a) 749 nm and (b) 610 nm at a wavelength of 1533 nm. (c) Allan deviation of the system based on IMS and DAS versus averaging time τ .

absorbance of 0.0002, accounting for a modest 1.3% of the overall absorbance. Consequently, the absorption of the two strip waveguides can be safely disregarded. Based on the measured absorbance and concentration, the group indices of the 2D PCW and 1D PCW are estimated to be 114 and 18, respectively.

B. Comparison of DAS and IMS

Figure 7(c) shows the Allan deviation analysis of the system based on direct absorption spectroscopy (DAS) and intensity modulation spectroscopy (IMS), where the 2D PCW serves as the sensing waveguide. The 1σ noise of the system amounts to 740 μV and 200 μV , indicating that the low-frequency noise can be suppressed by employing an AOM for intensity modulation with the fixed modulation frequency of 40 kHz, thereby improving the SNR by 3.7 times. Moreover, unlike choppers, the AOM does not add any supplementary noise from fiber alignment and mechanical noise. The sensor noise may originate from fluctuations in the laser power, airflow disturbance, and shot noise associated with the NIR detector. The sensor noise can also be suppressed by some denoising or filtering

algorithms; e.g., wavelet denoising and Savitzky–Golay filtering algorithms [40].

C. Group Index Measurement

To verify the accuracy of the findings, we established a Mach–Zehnder interferometer (MZI) with SMFs incorporating an amplified spontaneous emission (ASE) light source and an optical spectrum analyzer (OSA; AQ6370D, Yokogawa), which enabled measurement of n_g . The measurement setup is shown in Fig. 8(a). The variable optical attenuator (VOA) is used for a power match between the two MZI arms. By adjusting the coupling distance between the collimator and the SMF through a precision displacement table, the optical path difference can be changed. Figure 8(b) displays the interference fringes of the MZI based on the 2D PCW, where a phase difference of 2π corresponds to the two peaks of the interference spectrum. When the wavelength range is from 1528 nm to 1533.1 nm, the spacing between the resonant peaks becomes increasingly dense. Figure 8(c) is a local part of Fig. 8(b). When the waveguide length is 200 μm , the wavelength difference between adjacent interference fringes is 0.072 nm. Thus, the initial optical path difference between the two arms is 32.6 mm. As the length of the reference arm is increased, the fringes become denser, indicating that the optical path of the reference arm is longer. When the length of the waveguide is 1000 μm , it was observed that the optical path of the waveguide arm became longer, and the wavelength difference between the adjacent interference fringes changed to 0.056 nm. At this point, the distance between the collimator and the SMF increased by 9 mm compared to the initial distance. The value of $\Delta\lambda_2 = 0.056 \text{ nm}$ is the result of the combined effect of increasing the 2D PCW length by 800 μm and the increase in the free-space optical path of 9 mm, with an initial optical path difference of 32.6 mm. According to $n_g(\lambda) = \lambda^2 / (\Delta\lambda \times L)$ [41,42], where $\Delta\lambda$ is defined as the wavelength difference between two adjacent peaks of the interference spectrum, n_g is obtained as 104.5.

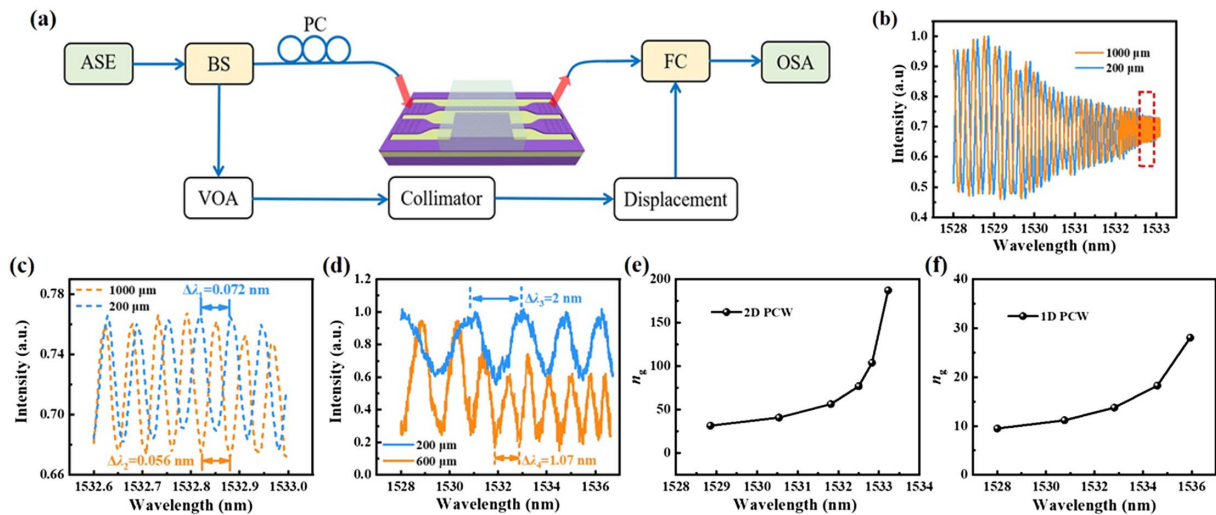


Fig. 8. (a) Experimental setup to measure n_g . BS, beam splitter; FC, fiber coupler. Interference fringes when the lengths of the 2D PCW are 200 μm and 1000 μm , where the wavelength range is (b) 1528–1533 nm and (c) 1532.6–1533.0 nm. Interference fringes when the lengths of the 1D PCW are 200 μm and 600 μm , where the wavelength range is 1528–1536.5 nm. Curves show the group index versus the wavelength for (e) the 2D PCW and (f) the 1D PCW.

Table 1. Comparison of the 2D PCW, the 1D PCW, and the Reported Waveguide Gas Sensors^a

Refs.	Waveguide	λ (μm)	L (cm)	f	n_g	γ	SLBW (nm)	α (dB/cm)	LoD (ppm)
This work	2D PCW	1.53	0.1	6%	114	6.84	27	44	277 (C ₂ H ₂)
	1D PCW	1.53	0.1	16%	18	2.88	10	10	706 (C ₂ H ₂)
[19]	Strip	1.65	10	—	—	0.254	—	2	772 (CH ₄)
[22]	Strip	4.24	0.32	—	—	0.44	—	3	NM (CO ₂)
[12]	Strip	4.26	1	—	—	0.195	—	4	NM (CO ₂)
[14]	Rib	2.57	2	—	—	1.07	—	6.8	40 (C ₂ H ₂)
[26]	SWG	6.65	2.84	—	—	0.24	—	3.9	25 (C ₇ H ₈)
[43]	SWG	7.33	1	—	—	1.13	—	4.7	10 (acetone)
[28]	SWG	6.15	0.3	10%	15	1.5	—	4.1	5 (NH ₃)

^a L , waveguide length; SLBW, slow light bandwidth; and NM, not mentioned.

Similarly, the interference fringes of the MZI based on the 1D PCW are shown in Fig. 8(d). For a waveguide length of 200 μm , the initial wavelength difference is 2 nm, while it is 1.07 nm with a length of 600 μm . $\Delta\lambda_4 = 1.07$ nm is caused by an increase in the length of the 1D PCW by 400 μm and an increase of 3 mm in the free-space optical path, with respect to the initial optical path. As a result, $n_g = 16.3$. There is an error of approximately 10% in the calculation of the n_g obtained via absorbance, which is in good agreement with the gas detection results. The error could be caused by fluctuations in the gas concentration and the inaccurate measurement of spectral density of interference fringes. The group index curves of the 2D and 1D PCWs extracted from the interference spectra are shown in Figs. 8(e) and 8(f), respectively.

D. Comparison of the Proposed 1D/2D PCW and Other Waveguide Gas Sensors

Table 1 shows the overall comparison of the slow light characteristics of the 2D PCW and the 1D PCW. The most remarkable difference is that the group index of 2D PCW reaches 114, which is 6.3 times that of the 1D PCW, resulting in an effective increase in the optical path by slowing down the light speed. However, the 2D PCW suffered from high propagation loss. The filling factor of the 1D PCW is approximately 2.7 times that of the 2D PCW due to its larger air hole area and smaller waveguide width. The slow light bandwidth, defined as a wavelength range when $n_g > 10$, is calculated through the dispersion structure of the PCWs. The slow light bandwidth of 2D PCW is 27 nm, while the 1D PCW has only 10 nm bandwidth, signifying greater ease in achieving a slow light effect and tolerance for errors in the 2D PCW. With a length of 1 mm, the ultraslow light performance of the 2D PCW allows it to reach a lower LoD. However, high propagation loss may restrict its application in NIR absorption spectroscopy since the waveguide must be very short. Despite the fact that the suspended strip waveguide [22] and suspended rib waveguide [14] may possess a relatively significant γ , they need a comparatively complex manufacturing process with inferior structural robustness. The nonsuspended strip waveguides [12,19] showed the lowest loss, with γ being only approximately 20%. The SWGs [26,43] demonstrated lower transmission losses, but the reported maximum γ is 150% [28]. In contrast, the 1D PCW boasted low propagation loss compared to the 2D PCW and an extraordinary interaction factor of up to 288%, which exhibits incomparable merits in gas detection.

When we consider the photodetector noise and the intensity noise of the laser, the LoD of the PCW gas sensor can be expressed as [24,43]

$$\text{LoD} \approx \frac{\text{SNR}_{\min} \cdot (\text{NEP} \sqrt{B} + k \cdot P_0)}{\gamma \cdot \alpha_g L \cdot P_0 \exp(-\alpha L)}, \quad (2)$$

where SNR_{\min} is the minimum detectable SNR of the sensor; P_0 is the injected power into the waveguide; k refers to the coefficient related to intensity noise of the laser; NEP and B are the noise equivalent power and bandwidth of the photodetector, respectively; L is the waveguide length; α is the propagation loss of the PCW; α_g is absorption coefficient of the gas analytes; and γ is the interaction factor.

LoD is inversely proportional to the interaction factor γ and absorption coefficient α_g , while also being influenced by a fluctuation in the laser power, the NEP, and the bandwidth of the photodetector. To minimize the LoD, it is imperative to maximize γ and select a strong absorption line (i.e., large α_g). Under the same input power P_0 , LoD increases with an increase in α . Therefore, for a PCW sensor with a high propagation loss, the waveguide length L can be shortened; otherwise, the input power must be amplified.

Compared to the waveguide sensor in Ref. [19], which is also an NIR sensor, the absorption coefficient of C₂H₂ was found to be 2.2 times higher than that of CH₄, but the PCW length was 100 times shorter. Despite this, we successfully realized a lower LoD, which stems from two factors: the ultrahigh interaction factor enabled by the compact design of the PCWs and the implementation of intensity modulation spectroscopy to effectively suppress the low-frequency noise inherent to the sensor. However, compared to other mid-IR waveguide sensors [26,28], which usually have absorption coefficients of 2–3 orders of magnitude larger than those in the near-IR, the reported PCW sensors show a higher LoD in general.

5. CONCLUSION

In summary, we demonstrated the NIR on-chip gas sensing capabilities of the 2D PCW and the 1D PCW, and suppressed the noise of the sensor by implementing an AOM to modulate the laser beam at a high frequency. The designed 2D PCW exhibited a group index of up to 114, with a detection limit of 277 ppm for C₂H₂ when the waveguide length was 1 mm. Although the 1D PCW did not perform in LoD as well as the former, the lower propagation loss and an extraordinary

interaction factor make it a more promising structure for an on-chip gas sensor with large scale integration than both the 2D PCW and the reported SWGs.

Funding. National Natural Science Foundation of China (62175087, 62235016, 61960206004); Key Science and Technology RD Program of Jilin Province, China (20200401059GX, 20230201054GX); Science and Technology Research Project of Department of Education, Jilin Province, China (JJKH20211088KJ); Program for JLU Science and Technology Innovative Research Team (JLUSTIRT, 2021TD-39).

Disclosures. The authors declare no conflicts of interest.

Data Availability. Data underlying the results presented in this paper are not publicly available at this time but may be obtained from the authors upon reasonable request.

REFERENCES

1. J. Smulko and M. Trawka, "Gas selectivity enhancement by sampling-and-hold method in resistive gas sensors," *Sens. Actuators B* **219**, 17–21 (2015).
2. Z. Li, X. Gui, C. Hu, L. Zheng, H. Wang, and J. Gong, "Optical gas sensor based on gas conjugated interference light source," *IEEE Photon. Technol. Lett.* **27**, 1550–1552 (2015).
3. Y. Jeong, J. Shin, Y. Hong, M. Wu, S. Hong, K. C. Kwon, S. Choi, T. Lee, H. Jang, and J. Lee, "Gas sensing characteristics of the FET-type gas sensor having inkjet-printed WS₂ sensing layer," *Solid-State Electron.* **153**, 27–32 (2019).
4. S. Zheng, H. Cai, L. Xu, N. Li, Z. Gu, Y. Zhang, W. Chen, Y. Zhou, Q. Zhang, and L. Lee, "Silicon substrate-integrated hollow waveguide for miniaturized optical gas sensing," *Photon. Res.* **10**, 261–268 (2022).
5. L. Hu, C. Zheng, D. Yao, D. Yu, Z. Liu, J. Zheng, Y. Wang, and F. K. Tittel, "A hollow-core photonic band-gap fiber based methane sensor system capable of reduced mode interference noise," *Infrared Phys. Technol.* **97**, 101–107 (2019).
6. J. Li, G. Luo, Z. Du, and Y. Ma, "Hollow waveguide enhanced dimethyl sulfide sensor based on a 3.3 μm interband cascade laser," *Sens. Actuators B* **255**, 3550–3557 (2018).
7. K. Zheng, C. Zheng, J. Li, N. Ma, Z. Liu, Y. Zhang, Y. Wang, and F. K. Tittel, "Near-infrared methane sensor system using off-axis integrated cavity output spectroscopy with novel dual-input dual-output coupling scheme for mode noise suppression," *Sens. Actuators B* **308**, 127674 (2020).
8. M. Pi, C. Zheng, H. Zhao, Z. Peng, J. Lang, J. Ji, L. Liang, Y. Zhang, Y. Wang, and F. K. Tittel, "Mid-infrared ChG-on-MgF₂ waveguide gas sensor based on wavelength modulation spectroscopy," *Opt. Lett.* **46**, 4797–4800 (2021).
9. C. Ranacher, C. Consani, N. Vollert, A. Tortschanoff, M. Bergmeister, T. Grille, and B. Jakoby, "Characterization of evanescent field gas sensor structures based on silicon photonics," *IEEE Photon. J.* **10**, 2700614 (2018).
10. M. S. Yazici, B. Dong, D. Hasan, F. Sun, and C. Lee, "Integration of MEMS IR detectors with MIR waveguides for sensing applications," *Opt. Express* **28**, 11524–11537 (2020).
11. C. Consania, C. Ranachera, A. Tortschanoffa, T. Grilleb, P. Irsiglerb, and B. Jakoby, "Mid-infrared photonic gas sensing using a silicon waveguide and an integrated emitter," *Sens. Actuators B* **274**, 60–65 (2018).
12. C. Ranachera, C. Consania, A. Tortschanoffa, R. Jannesarib, M. Bergmeisterc, T. Grillec, and B. Jakoby, "Mid-infrared absorption gas sensing using a silicon strip waveguide," *Sens. Actuators A* **277**, 117–123 (2018).
13. N. Singh, A. Casas-Bedoya, D. D. Hudson, A. Read, E. Mägi, and B. J. Eggleton, "Mid-IR absorption sensing of heavy water using a silicon-on-sapphire waveguide," *Opt. Lett.* **41**, 5776–5779 (2017).
14. M. Vlk, A. Datta, S. Alberti, H. D. Yallev, V. Mittal, S. C. Factor, G. S. Murugan, J. Jágerská, and S. C. Factor, "Extraordinary evanescent field confinement waveguide sensor for mid-infrared trace gas spectroscopy," *Light Sci. Appl.* **10**, 26 (2021).
15. B. Schwarz, P. Reininger, D. Ristanic, H. Detz, A. M. Andrews, W. Schrenk, and G. Strasser, "Monolithically integrated mid-infrared lab-on-a-chip using plasmonics and quantum cascade structures," *Nat. Commun.* **5**, 4085 (2014).
16. Q. Guo, J. Zhang, K. Yang, Y. Zhu, Q. Lu, N. Zhuo, S. Zhai, J. Liu, L. Wang, S. Liu, and F. Liu, "Monolithically integrated mid-infrared sensor with a millimeter-scale sensing range," *Opt. Express* **30**, 40657–40665 (2022).
17. B. Hinkov, F. Pilat, L. Lux, P. L. Souza, M. David, A. Schwaighofer, D. Ristanic, B. Schwarz, H. Detz, A. M. Andrews, B. Lendl, and G. Strasser, "A mid-infrared lab-on-a-chip for dynamic reaction monitoring," *Nat. Commun.* **13**, 4753 (2022).
18. N. A. Mortensen and S. Xiao, "Slow-light enhancement of Beer-Lambert-Bouguer absorption," *Appl. Phys. Lett.* **90**, 141108 (2007).
19. L. Tombez, E. J. Zhang, J. S. Orcutt, S. Kamapurkar, and W. M. J. Green, "Methane absorption spectroscopy on a silicon photonic chip," *Optica* **4**, 1322–1325 (2017).
20. M. Pi, C. Zheng, R. Bi, H. Zhao, L. Liang, Y. Zhang, Y. Wang, and F. K. Tittel, "Design of a mid-infrared suspended chalcogenide/silica-on-silicon slot-waveguide spectroscopic gas sensor with enhanced light-gas interaction effect," *Sens. Actuators B* **297**, 126732 (2019).
21. M. Pi, C. Zheng, J. Ji, H. Zhao, Z. Peng, J. Lang, L. Liang, Y. Zhang, Y. Wang, and F. K. Tittel, "Surface-enhanced infrared absorption spectroscopic chalcogenide waveguide sensor using a silver island film," *ACS Appl. Mater. Interface* **13**, 32555–32563 (2021).
22. F. Ottonello-Briano, C. Errando-Herranz, H. Rödjegård, H. Martin, H. Sohlström, and K. Gylfason, "Carbon dioxide absorption spectroscopy with a mid-infrared silicon photonic waveguide," *Opt. Lett.* **45**, 109–112 (2020).
23. A. Rostamian, E. Madadi-Kandjani, H. Dalir, V. J. Sorger, and R. T. Chen, "Towards lab-on-chip ultrasensitive ethanol detection using photonic crystal waveguide operating in the mid-infrared," *Nanophotonics* **10**, 1675–1682 (2021).
24. A. Gervais, P. Jean, W. Shi, and S. LaRochelle, "Design of slow-light subwavelength grating waveguides for enhanced on-chip methane sensing by absorption spectroscopy," *IEEE J. Sel. Top. Quantum Electron.* **25**, 5200308 (2019).
25. W. C. Lai, S. Chakravarty, Y. Zou, and R. T. Chen, "Multiplexed detection of xylene and trichloroethylene in water by photonic crystal absorption spectroscopy," *Opt. Lett.* **38**, 3799–802 (2013).
26. W. Liu, Y. Ma, Y. Chang, B. Dong, J. Wei, Z. Ren, and C. Lee, "Suspended silicon waveguide platform with subwavelength grating metamaterial cladding for long-wave infrared sensing applications," *Nanophotonics* **10**, 1861–1870 (2021).
27. L. Sun, Y. Zhang, Y. He, H. Wang, and Y. Su, "Subwavelength structured silicon waveguides and photonic devices," *Nanophotonics* **9**, 1321–1340 (2020).
28. K. M. Yoo, J. Midkiff, A. Rostamian, C. J. Chung, H. Dalir, and R. T. Chen, "InGaAs membrane waveguide: a promising platform for monolithic integrated mid-infrared optical gas sensor," *ACS Sens.* **5**, 861–869 (2020).
29. W. C. Lai, S. Chakravarty, X. Wang, C. Lin, and R. T. Chen, "On-chip methane sensing by near-IR absorption signatures in a photonic crystal slot waveguide," *Opt. Lett.* **36**, 984–986 (2011).
30. Y. Zou, S. Chakravarty, P. Wray, and R. T. Chen, "Mid-infrared holey and slotted photonic crystal waveguides in silicon-on-sapphire for chemical warfare simulant detection," *Sens. Actuators B* **221**, 1094–1103 (2015).
31. K. Qin, S. Hu, S. T. Retterer, I. I. Kravchenko, and S. M. Weiss, "Slow light Mach-Zehnder interferometer as label-free biosensor with scalable sensitivity," *Opt. Lett.* **41**, 753–756 (2016).
32. N. R. Ramanujam, A. Panda, P. Yupapin, A. Natesan, and P. Prabpal, "Numerical characterization of 1D-photonic crystal waveguide for

- female reproductive hormones sensing applications,” *Physica B* **639**, 414011 (2022).
33. R. R. Singh and V. Priye, “Silicon nanowire optical rectangular waveguide biosensor for DNA hybridization,” *IEEE Photon. Technol. Lett.* **30**, 1123–1126 (2018).
 34. <https://refractiveindex.info>.
 35. J. T. Robinson, L. Chen, and M. Lipson, “On-chip gas detection in silicon optical microcavities,” *Opt. Express* **16**, 4296–4301 (2008).
 36. W. Yang, X. Chen, X. Shi, and W. Lu, “Selective modes excitation in multimode photonic crystal waveguides,” *Superlattices Microstruct.* **49**, 74–80 (2011).
 37. J. Tan, M. Lu, A. Stein, and W. Jiang, “High-purity transmission of a slow light odd mode in a photonic crystal waveguide,” *Opt. Lett.* **37**, 3189–3191 (2012).
 38. X. Chen and H. K. Tsang, “Polarization-independent grating couplers for silicon-on-insulator nanophotonic waveguides,” *Opt. Lett.* **36**, 796–798 (2011).
 39. X. Xu, H. Subbaraman, J. Covey, D. Kwong, A. Hosseini, and R. T. Chen, “Complementary metal–oxide–semiconductor compatible high efficiency subwavelength grating couplers for silicon integrated photonics,” *Appl. Phys. Lett.* **101**, 031109 (2012).
 40. J. Ji, Y. Huang, M. Pi, H. Zhao, Z. Peng, C. Li, Q. Wang, Y. Zhang, Y. Wang, and C. Zheng, “Performance improvement of on-chip mid-infrared waveguide methane sensor using wavelet denoising and Savitzky-Golay filtering,” *Infrared Phys. Technol.* **127**, 104469 (2022).
 41. Y. A. Vlasov, M. O’Boyle, H. F. Hamann, and S. J. McNab, “Active control of slow light on a chip with photonic crystal waveguides,” *Nature* **438**, 65–69 (2005).
 42. J. Y. Lee and P. M. Fauchet, “Slow-light dispersion in periodically patterned silicon microring resonators,” *Opt. Lett.* **37**, 58–60 (2012).
 43. W. Liu, Y. Ma, X. Liu, J. Zhou, C. Xu, B. Dong, and C. Lee, “Larger-than-unity external optical field confinement enabled by metamaterial-assisted comb waveguide for ultrasensitive long-wave infrared gas spectroscopy,” *Nano Lett.* **22**, 6112–6120 (2022).